Electrochemical Conversion of Methane to Ethylene, Olefins, and Paraffins Using Metal-Supported Solid Oxide Cells

Boxun Hu, Fabian Rosner, Hanna Breunig, Asia Sarycheva, Robert Kostecki,

and Michael C. Tucker

Energy Storage and Distributed Resources, and Energy Analysis and Environmental Impacts Divisions, Lawrence Berkeley National Laboratory, Berkeley, CA 94720, USA

Abstract

Electrochemical oxidative coupling of methane (E-OCM) with $Sr_2Fe_{1.5}Mo_{0.5}O_{6-\delta}$ (SFM) catalyst is demonstrated with metal-supported solid oxide cells (MS-SOC). SFM anode and Pr_6O_{11} cathode catalysts are loaded into a porous symmetric-architecture cell by infiltration and firing. The most effective chelating agent (citric acid/ethyl glycol) and optimal firing/reducing temperatures (850°C/750°C) for the SFM catalyst precursor solution are selected and confirmed by cell testing. Operating temperature, cell voltage, and oxygen concentration at the cathode greatly affect the methane conversion rate and product selectivity by controlling the oxygen ion flow. CH_4 conversion of 85.8% is obtained, with C_2H_4, C_2H_6, and H_2 concentrations of 10.5%, 12.3%, and 25.6% at 800°C, respectively, in the product exhaust gas. Reasonable stability of the current density and methane conversion is demonstrated during 200 h operation. This research demonstrates technical progress in catalyst and device development for the E-OCM reaction to synthesize valuable chemicals.

Key words: electrochemical oxidative coupling of methane, $Sr_2Fe_{1.5}Mo_{0.5}O_{6-\delta}$, infiltration, metal-supported solid oxide cell, stability, ethylene

Phone 1-510-486-5304, Fax 1-510-486-4260

LBNL; 1 Cyclotron Rd; MS 62-203; Berkeley CA 94720; USA

1. Introduction

The conversion of simple organic carbon molecules, such as methane, to more valuable higher hydrocarbons and alkenes, including ethylene and propylene, continues to be a grand challenge [1]. Ethylene and propylene are consumed in high volumes to generate critical chemicals such as ethylene/propene oxide, ethylene glycol, polyethylene/propylene [2], and are currently produced from petrochemicals through CO_2-emitting and energy-intensive thermochemical processes [3]. In pursuit of alternate synthesis routes for the production of C2+ compounds, methanol to olefins (MTO), Fischer-Tropsch synthesis (FTS), catalytic dehydrogenation, and oxidative coupling of methane (OCM) have attracted the interest of the research community [4]. The advantages of each process in terms of catalysts, stability, cost, and CO_2 emission have been summarized by Amghizar et al [5]. In OCM, a high CH_4/O_2 ratio (>10) over solid catalysts is utilized to enhance the C_2 selectivity. Thermodynamically, however, CO_2 or solid carbon are the preferred products. Farrell et al. suggested that this thermodynamic constraint can be partially alleviated by employing membrane reactors, leading to recent interest in the use of electrochemical reactors for OCM [6]. Moreover, transitioning to electrochemical production pathways that can leverage low-carbon renewable energy to convert methane, whether fossil or biologically sourced, has potential to substantially lower greenhouse gas emissions from the chemical industry. De Luna et al. recently reviewed the displacement of petrochemical processes by renewably powered electrosynthesis, finding that high-value renewables, such as ethylene, can be made with a net negative carbon emissions footprint when powered by renewable electricity [7].

Electrochemical oxidative coupling of methane (E-OCM) to ethylene in a solid oxide cell (SOC) reactor was recently demonstrated at lab-scale [8, 9]. Compared to the conventional fixed-bed OCM reactor, an oxygen-selective SOC membrane reactor eases the cost and safety concerns by

eliminating the requirement of an expensive air separation unit, and eliminating the direct co-feeding of explosive methane-oxygen mixtures [10]. E-OCM combines the advantages of OCM catalysts and membrane reactors; a controlled flow of oxygen ion is driven across the oxygen-ion conducting electrolyte to activate methane by a bias [11, 12]. In addition to the oxide-conducting devices studied in this work, proton-conducting fuel cells are also pursued for ethylene and propane synthesis via nonoxidative hydrogenation mechanisms [13-15]. However, oxygen-ion conducting membranes offer advantages with respect to oxidant selection. Instead of using air, in E-OCM, oxygen can be also provided by reducing CO_2 to CO or by co-producing H_2 from steam [8, 16]. This type of co-production is particularly attractive as it leverages capital expenditures as well as operating costs.

Various OCM catalysts, such as $(Pr_{0.3}Sr_{0.7})_{0.9}Ni_{0.1}Ti_{0.9}O_3$ and Mn-Ce-Na_2WO_4 have been explored for OCM to olefins [10, 17]. Molybdenum-doped strontium ferrite (SFM) has been selected as the leading E-OCM catalyst due to its excellent mixed conductivity, coking-resistance, and methane coupling efficiency [8, 9, 18, 19]. The ease with which SFM forms oxygen vacancies and allows for facile bulk oxide ion diffusivity arises from its impressive mixed ionic and electronic conductivity [20]. Exsolved iron nanoparticles can form on the SFM perovskite matrix anode under reducing environment, enhancing the catalytic activity and stability [21]. The Fe/SFM interface promotes the key step of the first cleavage of C–H bonding in CH_4 and then the selective coupling of methane for C_2H_4 generation [9]. Compared to conventional Ni-based SOC electrodes, the SFM anode is much less active for the hydrogen oxidation (Eq.1), methane steam reforming (Eq. 2), and water-gas shift reaction (Eq. 3) side reactions, and thus increases the selectivity for OCM to ethylene (Eq. 4) and other olefins and paraffins.

$$H_2\,(g) + O^{2-} \rightarrow H_2O\,(g) + 2e^- \qquad (1)$$

CH_4 (g) + H_2O (g) → 3H_2 (g) + CO (g) (2)

CO (g) + H_2O (g) → CO_2 (g) + H_2 (g) (3)

$2CH_4$ (g) + $2O^{2-}$ → C_2H_4 (g) + $2H_2O$ (g) + $4e^-$ (4)

Metal supported solid oxide cells (MS-SOC) exhibit fast start up, excellent mechanical stability, and tolerance to intermittent operation, making them compatible with dynamic renewable energy sources [22, 23]. Moreover, metal supported cells offer advantages with respect to system integration. In ethylene plants, the downstream product separation necessitates a cell outlet pressure of approximately 1.7 bar [24, 25]. Conventional cell architectures require equal pressures on anode and cathode, demanding energy- and capital-intensive air compression on the cathode side combined with a highly accurate and fast-acting control system. MS-SOCs on the other hand are able to tolerate large pressure differentials between anode and cathode compartments due to their excellent mechanical stability [26]. This could allow air to be supplied at close to ambient pressure, reducing power consumption, system complexity and costs, and making MS-SOCs the preferred choice for E-OCM. This system design flexibility also translates to other scenarios, e.g. H_2 co-production, where elevated pressure H_2 production can reduce downstream H_2 compression power (H_2 will need to be compressed for shipping or pipeline). Due to these reasons MS-SOCs for E-OCM are of major interest and in this work, E-OCM with MS-SOCs is demonstrated for the first time. The porous symmetric electrode/support structure allows various electrode catalysts to be introduced via infiltration for high performance cells [27, 28]. Pr_6O_{11} is an excellent catalyst for oxygen reduction, and is infiltrated as the cathode catalyst here. Addition of Pr_6O_{11} to standard SOFC cathode materials increases the surface oxygen exchange rate and cell performance[29, 30]. Our previous study shows that pure Pr_6O_{11} cathode catalyst was more active than the conventional lanthanum strontium manganite (LSM) cathode catalyst in MS-SOFCs [31]. Metal-supported solid

oxide fuel cells with infiltrated Pr_6O_{11} electrode have demonstrated a high cell performance (0.9 W cm^{-2} at 700°C in hydrogen fuel [28]. In this study, SFM catalyst and Pr_6O_{11} were infiltrated into the SSZ scaffolds by a fast infiltration process to form a complete cell (Figure 1). The phase purity of SFM at various temperatures for the air-firing and reduction process in air and hydrogen was investigated by high temperature X-ray diffraction (HT-XRD). The impact of cell voltage, operating temperature, and flow rates on the E-OCM reaction are determined. The stability of the MS-SOC over 200 h operation is demonstrated. The metal-supported SFM-ScSZ‖ScSZ‖ScSZ-Pr_6O_{11} cell demonstrated here advances the possibility of ethylene production at intermediate temperature integrated with renewable energy.

2. Experimental Methods

2.1. Cell Fabrication and Testing

Cell preparation

The cell preparation was adapted from our previous procedures for this new application, with the metal-ceramic cell structure unchanged, and the infiltration process modified for SFM deposition [28]. Symmetrical metal-supported button cells (~2.5 cm diameter) were prepared from P434L stainless steel powder (Ametek, USA) and scandium doped zirconia (ScSZ) powder via tape casting, lamination, laser cutting, debinding, and sintering at 1350°C for 2 h in 2% H_2 to achieve dense electrolyte and porous electrodes by standard methods. Then the cells were fired in air at 850°C for 6 hours to increase the metal support wettability for infiltration. Before each infiltration of electrode catalysts, acrylic paint (Liquitex) covered the edge of the cell to prevent catalyst deposition on the perimeter area. To prepare $Sr_2Fe_{1.5}Mo_{0.5}O_{6-\delta}$ (SFM) solution,

stoichiometric mixtures of Sr-, Mo-, and Fe-nitrates (Sigma Aldrich, Sr: Fe: Mo = 5:3.75:1.25 mmol) were mixed with Triton-X surfactant/water (10:1, 10 g), and chelating agents (20 mmol, citric acid/ ethyl glycol (EG) (1:1 mol ratio, Sigma Aldrich). Further information on selection of the chelating agent is provided in the supplemental information (SI). The intended final composition is $Sr_2Fe_{1.5}Mo_{0.5}O_{6-\delta}$. Ammonia solution (Sigma Aldrich, 25%) was added to adjust the pH solution to near 7 (checked by pH paper). Pr nitrate solution and SFM solution were dripped onto the cathode and anode sides, respectively, mild vacuum was applied to remove air from the cell, excess surface solution was wiped off, and the solutions were dried at 90°C for 10 minutes. The cells with infiltrated anode and cathode catalyst precursor solutions were fast-fired in a hot furnace (850°C) for 30 min each cycle to produce the catalyst oxides [32]. Pr-oxide cathode was infiltrated 8 cycles and SFM anode was infiltrated 3 cycles.

Cell testing

The cell structure and test setup are shown in Fig. 1. Button cells were mounted onto 410 stainless steel test rigs [33]. Pt mesh was spot welded to both sides of the cells and connected with a potentiostat (Biologic VMP3) by Pt wires. Glass powder (Schott G018-354 or GM31107) mixed with binder (Schott AG) was applied as a paste by syringe to the edges of the cells and heated to above 700°C at 3°C min^{-1} and cured for 1 h. The cell temperature was then ramped to the designated operating temperature at 10°C min^{-1}. The cell supported on a test rig was enclosed in an alumina tube (2" diameter, bottom end open). The open end was filled with insulating alumina wool (Zircar).

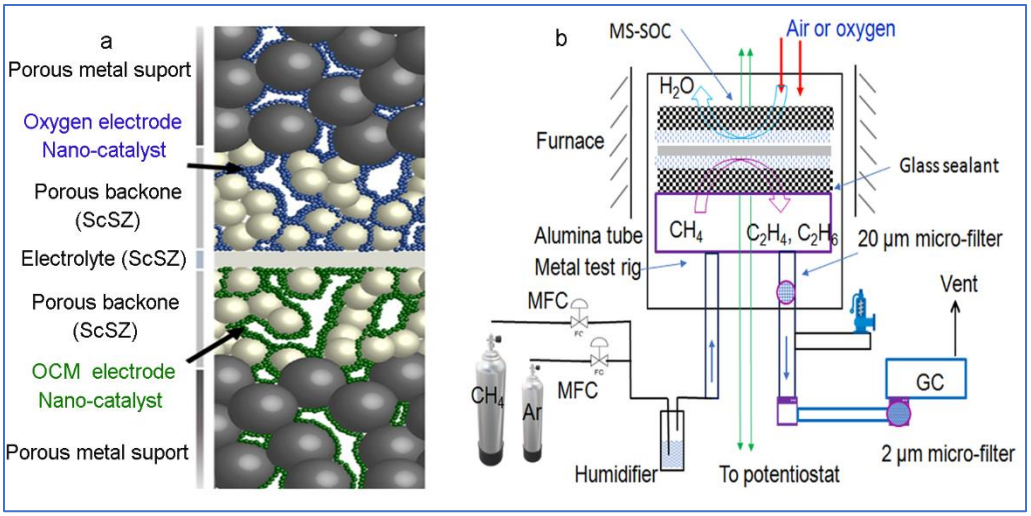

Fig. 1. Experimental setup. Schematic of a) cell structure, adapted with permission from Reference [34] and b) experimental setup for electrochemical coupling of methane to ethane/ethylene. Details of the cell and catalysts are shown in Fig. 7.

The anode was reduced by 3% H_2 in Ar in the range 750 to 900°C for 15 h before introducing fuel mixed with 10 v% Ar as an internal standard gas for GC analysis. The fuel gas flowing at 120 cm^3 min^{-1} was typically 90% CH_4/10% H_2O (methane fuel), and 97% H_2/3% H_2O (hydrogen fuel) was used in some cases to determine fuel cell performance. The cathode was exposed to air or oxygen flowing at 600 cm^3 min^{-1}. Open circuit voltage (OCV), cyclic voltammetry (CV) from OCV to OCV-1.8 V, electrochemical impedance spectroscopy (EIS) and cell performance (IV-PI and I-t) were recorded with a multichannel potentiostat with current boosters (Biologic VMP3 with 10 A boosters). The anode exhaust gas line passed to a gas chromatograph (GC) for product analysis. Microfilters (20 µm and 2 µm stainless steel) were placed between the cell and GC to avoid blocking the GC columns by carbon/catalyst particles.

2.2 Characterization

To prepare samples for x-ray diffraction (XRD) analysis, SFM infiltration solution was dried at 90°C and then fired at 400°C or higher in air to avoid poisonous NO_2 gas release in the high-temperature XRD instrument. To optimize the firing temperature, a high temperature-XRD (HT-XRD, Rigaku) with an automated multipurpose X-ray diffractometer equipped with an Anton Paar high-temperature oven chamber and SmartLab Studio II software was utilized to analyze the phase change in air during the firing process. The SFM powder fired in air up to 900°C. The dwell time for each temperature was 10 min. Reduction in hydrogen requires a long time and it was not fit for HT-XRD. Therefore, three SFM powders were reduced in a tube furnace at 750°C, 850°C, and 900°C in 3% H_2/Ar for 10 h before room-temperature x-ray diffraction (XRD, Bruker D2 Phaser) analysis with a scanning speed of 5° min^{-1} at a step size of 0.02°.

Pretest and posttest cell samples were mounted in epoxy, cut, and polished to prepare for scanning electron microscope (SEM) analyses. A Zeiss Gemini Ultra-55 SEM at a voltage of 20 kV with an energy dispersive X-ray (EDX) detector was utilized to obtain field emission scanning electron microscopy (FESEM) images and element maps. After operation, the metal supports were peeled apart and the SFM-ScSZ electrode was analyzed for carbon deposition using a Renishaw InVia Qontor Raman system spectrometer with 433 nm and 633 nm lasers equipped with 50x magnification lens.

An online GC (SRI 8610C) was utilized to analyze the products of the anode outlet. The inlet and outlet gas lines were heated above 120°C using heating tape. The GC was equipped with a HaySep D column, a TCD detector for CO and water analysis, a methanizer, and an FID detector for hydrogen, CO_2, and hydrocarbon analysis. The oven temperature was set at 40°C for 10 mins and then ramped at 20°C/min to 210°C for 6 mins. A certified reformate gas mixture (69.8 v% H_2, 1.3 v% CH_4, 15.7 v% CO, and 13.2 v% CO_2) and a C2/C3 mixture (20.3 v% C_2H_4, 9.6 v% C_2H_6,

4.97 v% C_3H_6, 3 v% C_3H_8, and Ar balance) were used to calibrate the GC. The method of hydrocarbon (C2 to C5) and water analysis is based on an earlier report [4].

3. Results and discussion

3.1 XRD/SEM study for optimal SFM firing and reducing temperature

In- and ex-situ analysis of the SFM catalyst guided selection of synthesis process conditions for cell fabrication. Pure perovskite SFM catalyst is typically produced by solid state processing at >1000°C in air [20, 35]. Metal-supported cells, however, cannot be exposed to air above about 900°C to avoid over-oxidation of the stainless steel. The phase purity of the SFM catalyst under this processing temperature constraint was evaluated by XRD, respectively. Optimal firing and reducing temperatures for infiltrated SFM catalyst were determined by combining the XRD/SEM study with E-OCM activity evaluation. After the SFM precursor solution was dried and fired at 400°C in air for 2 h, the major phase is $SrMoO_4$ (PDF: 085-0586), with small amounts of the intended perovskite $Sr_2FeMoO_{6-\delta}$ (PDF: 060-0459) and magnetite Fe_3O_4 (PDF: 87-2334) (Fig. 2a). Upon increasing the firing temperature from 400°C to 900°C in air, the $Sr_2FeMoO_{6-\delta}$ phase gradually disappeared and $SrMoO_4$ dominated the XRD pattern. At 750°C, the $Sr_2FeMoO_{6-\delta}$ peak at 19.5° fully disappeared. After firing in air at 850°C, the SFM catalyst consists primarily of doped $SrMoO_4$ and small amounts of Fe_3O_4 and $Sr_2FeMoO_{6-\delta}$. More XRD patterns at other intermediate temperatures and magnified XRD patterns fired in air at 850°C are shown in Fig. S1. In reducing environment, perovskite SFM catalyst can be obtained at a relatively low temperature. Fig. 2b shows that conversion of the $SrMoO_4$ phase to the desired perovskite SFM catalyst starts at 750°C and is mostly completed at 900°C in 3% H_2/Ar for 10 h.

To further determine the optimal firing/reducing temperature, several cells were fabricated at various air-firing (400 to 850°C) and reducing (750 to 900°C) temperatures and these cells were tested under the same E-OCM conditions. The results based on product analysis by GC showed that the best SFM synthesis protocol is air firing at 850°C, followed by reducing at 750°C, even though the pure perovskite SFM phase was not achieved (Figs. 2b and S1a, b). Further increasing the reducing temperature increased the SFM particle size, thereby decreasing catalyst surface area, leading to low catalyst activity. These results suggest there is a tradeoff between phase purity and surface area. It is challenging to simultaneously obtain the desired perovskite phase and high surface area SFM from infiltrated precursors at the relatively low temperature dictated by the metal support. Nevertheless, the mixed-phase SFM catalyst developed here was effective for the desired E-OCM reaction, as discussed below. It may be fruitful to further optimize the solution composition, chelating agents, and firing protocol in the future.

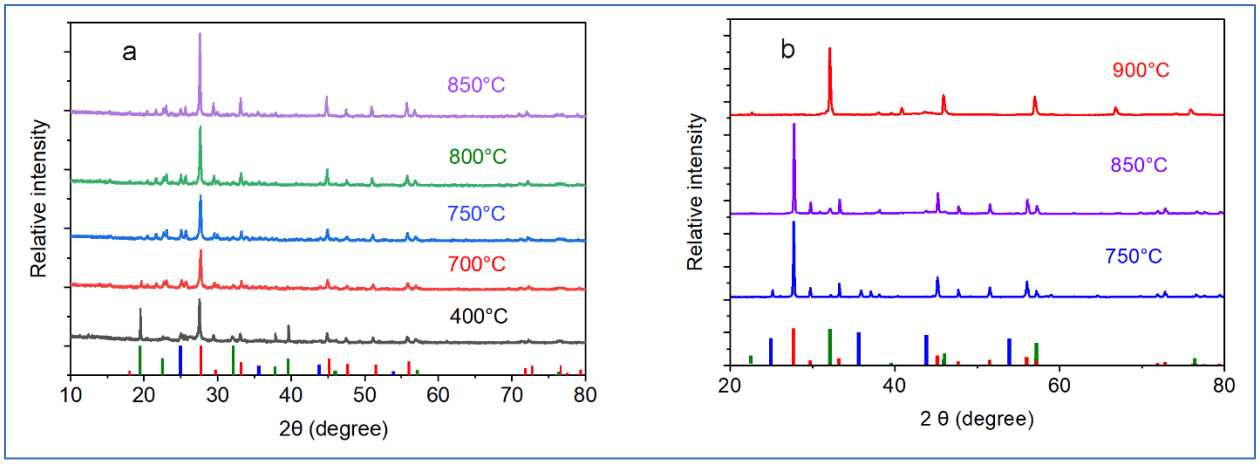

Fig. 2. XRD analysis of SFM phase purity and structure. a: HT-XRD patterns of SFM powder fired at 400 to 850°C in air. b: room temperature XRD patterns of SFM powder reduced in 3% H_2/Ar at temperatures of 750 to 900°C after firing at 850C°C in air. Standard patterns shown at

the bottom for $SrMoO_4$ (red, PDF: 085-0586), perovskite $Sr_2FeMoO_{6-\delta}$ (green, PDF: 060-0459) and magnetite Fe_3O_4 (blue, PDF: 87-2334).

3.2 Electrochemical characterization

First, to establish baseline performance, we assessed operation with hydrogen fuel. Then we studied E-OCM with methane fuel. Electrochemical characterization of the MS-SOCs (Fig. 3) shows relatively low hydrogen oxidation performance compared to standard SOFC catalysts, which is preferred to favor the E-OCM reaction. In fuel cell mode (hydrogen oxidation), the SFM anode-based MS-SOC shows a low maximum power of 0.12 W cm^{-2}, 0.2 W cm^{-2}, and 0.35 W cm^{-2} at 650°C, 700°C, and 750°C respectively in hydrogen fuel, Fig 3a. This performance is comparable to the 0.37 W/cm^2 peak power reported at 750ºC for electrolyte-supported Ni-doped SFM-GDC cells [36]. For comparison, Ni-CeO_2 anode-based MS-SOCs optimized for hydrogen oxidation (Eq 1) provide much higher peak power of 0.9 W cm^{-2} with hydrogen fuel [28], 0.4 W cm^{-2} with natural gas reformate fuel [37], and 0.5 W cm^{-2} with natural gas direct internal reforming [38] at 700°C. However, Ni-CeO_2 is not effective for the desired E-OCM reaction (Eq. 4): no C2 products were converted from CH_4 when a cell voltage of -0.93 V (Ewe) was applied (Fig. S2a). In fact, an anode catalyst such as SFM, with less activity in hydrogen oxidation reaction (HOR) and methane reforming, but active in OCM, is favored to maximize the selectivity and conversion of CH_4 to C_2 product. To pump oxygen to the anode for the E-OCM reaction, a large negative cell voltage was applied (Fig. 3b). The SFM shows low H_2 oxidation performance (0.2W/cm^2) relative to standard MS-SOFC anode (SDC-Ni, 0.9 W/cm^2). The even lower performance in methane is because the SFM composite is not a good reforming catalyst (which is desirable because reforming is a side reaction that does not contribute to C2+ production). Large current density with methane results in low (negative) cell voltage to drive oxygen consumption and transport across the

membrane, given the sluggish OCM reaction (compared to H_2 oxidation or CH_4 reforming in the presence of Ni). This is consistent with the previous SFM-OCM literature (for example Reference 9, Fig 3a which has a reverse sign convention). The low current at normal fuel cell operating voltage range, followed by larger current at negative operating voltage (large overpotential) is consistent with previous studies [9, 39]. From EIS analysis, the ohmic resistance was almost the same for hydrogen and methane, but the polarization resistance was much higher for methane (Fig. 3c). Distribution of relaxation times (DRT) analysis of the EIS spectra was performed using the open software and computing techniques developed by Ciucci and Chen et al., Fig 3d [40]. Four physico-chemical processes can be identified for both fuels, and the DRT peak positions for H_2 are consistent with those reported previously for Ca-doped SFM symmetrical SOC [41] and metal supported SOC [34]. The P1 peak at high frequency range (related to oxygen ion transport process) is overlapped for H_2 and CH_4, which is consistent with the overlapping EIS ohmic resistance. The surface exchange (P2), dissociation (P3 peak) and diffusion (P4 peak) of CH_4 are more resistive than those of H_2, consistent with the large overpotential at small current observed in Fig. 3b.

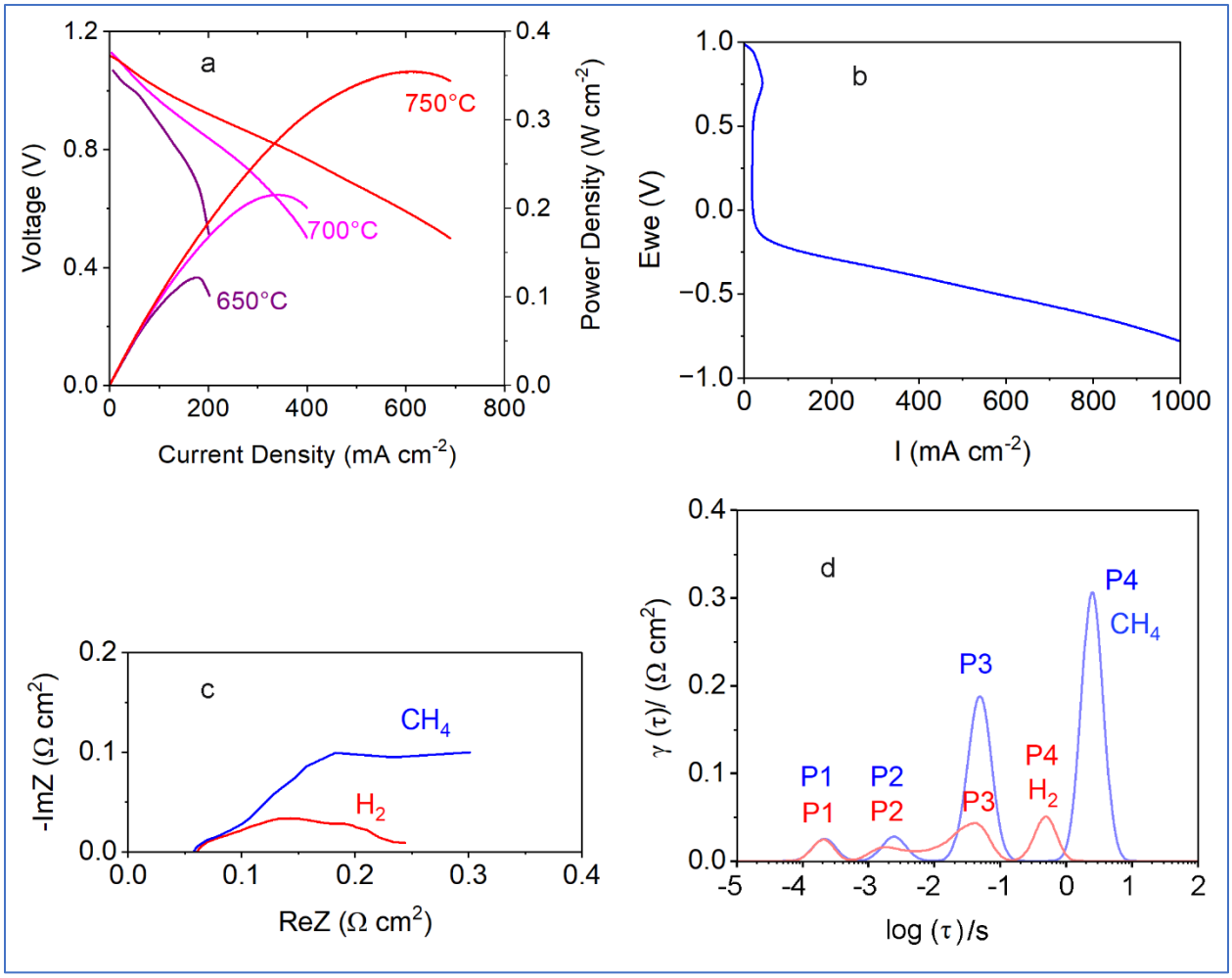

Fig. 3 Electrochemical characterization of the MS-SOCs. a: Fuel cell performance of SFM-based cell using hydrogen fuel and air, b: Polarization in methane fuel at 750°C, c: EIS spectra at 750°C and 0.7 V, d: corresponding DRT analysis of sub-figure c. Inlet methane fuel compositions: 90% CH_4 /10% H_2O.

3.3 Cell E-OCM operation and product analysis

Methane conversion rate and selectivity to C2+ products were sensitive to applied cell voltage, operating temperature, and methane flow rate. The calculation methods of methane conversion and selectivity are shown in the Supplemental Information. High conversion was achieved at negative

cell voltage, Fig 4a, b. The OCV with methane fuel was 0.87 V, consistent with the small amount of hydrogen generated by steam reforming. Note that the OCV at cell startup with hydrogen fuel was identical to the theoretical value (1.12 V), indicating excellent sealing and gas-tight electrolyte. The current density across the cell increased from 0.2 to 0.8 A cm^{-2} with cell voltage decreasing from -0.13 to -0.93 V (Fig. 4a and Fig. S3). Current density was stable at each voltage used for analysis, and GC samples were obtained after applying the bias for 10 mins to allow adequate purging of the anode chamber and tubes (Fig 4a). Significant conversion of methane to C2 products first appeared at -0.13 V. Methane conversion increased with decreasing voltage and reached 55.3 ± 2.7% at -0.93 V. The selectivity to C2 reached a maximum of 75.5 ± 3.8% at -0.53 V, and the C_2H_4/C_2H_6 ratio was about 1:8. A large negative bias increases the side reaction formation of CO_2 [39], and this is evident in the decreasing C2 selectivity below -0.53 V. Song et al reported that the C_2H_4 selectivity was reduced from 90.0% to 76.7% due to oxygen species formed at the anode when the current increased from 0 to 100 mA[42].

The E-OCM performance is quite sensitive to temperature in the range 650°C to 800°C (Fig. 4c). While C2 peaks appeared at 650°C, both the ethylene and ethane peaks increase dramatically with operating temperature. At 800°C, the CH_4 conversion increased to 83.4 ± 4.2%, with C2 selectivity of 72.1 ± 3.6%, and C_2H_4/C_2H_6 ratio around 1:3. At 750°C and above, the C2 selectivity did not keep pace with total CH_4 conversion due to more CO_2 formation via the competing reforming reactions (Eq. 2 and 3). Due to temperature limitation of the glass sealant, these MS-SOC cells were not operated at >800°C. Based on these results, 750 to 800°C was chosen as the operating temperature for more detailed analysis of product composition at low cell voltage, discussed below.

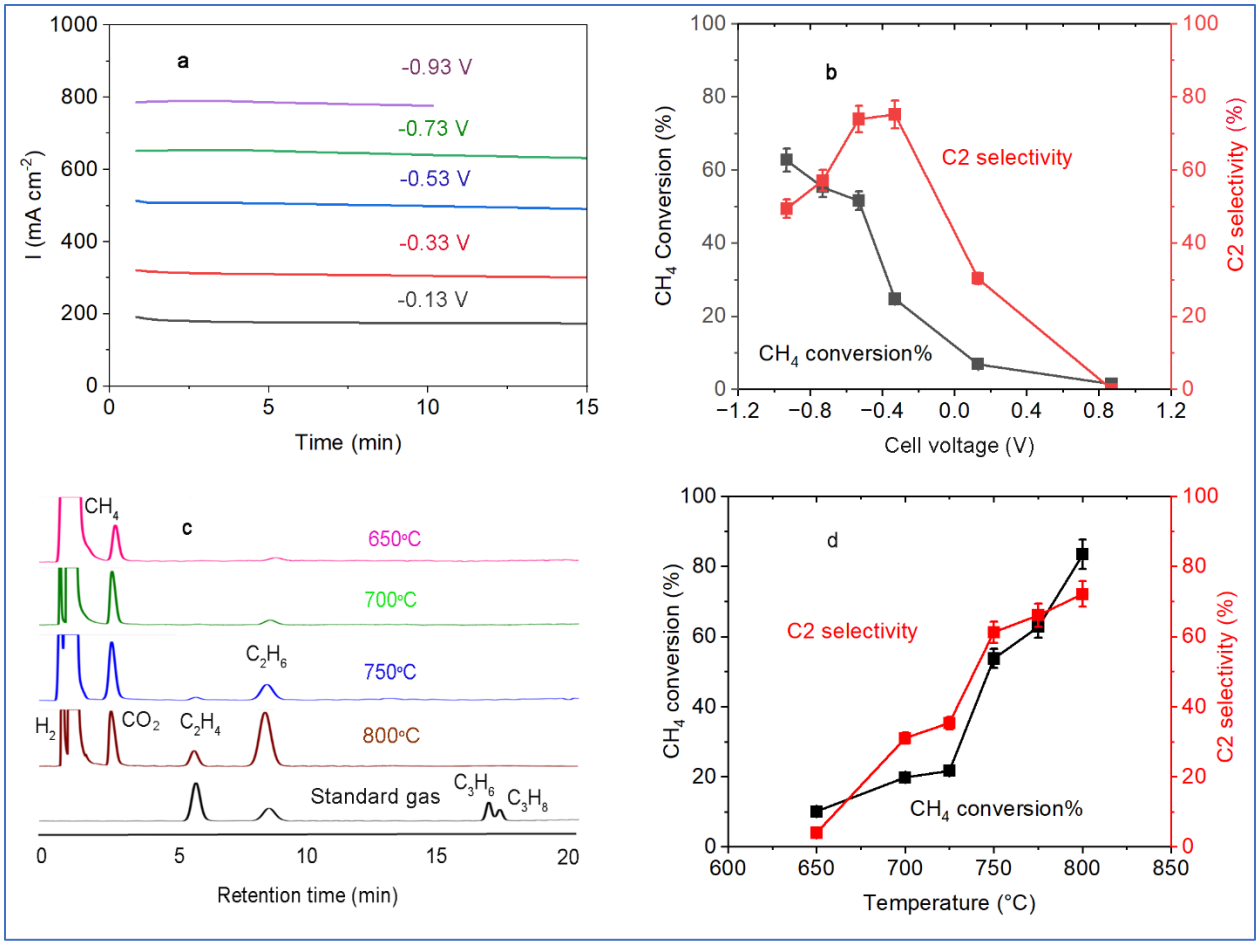

Fig. 4. Impact of operating temperature and cell voltage on E-OCM reaction. Inlet methane fuel compositions: 80% CH_4/10%/Ar/10% H_2O. a: Current density dependence on cell voltage. Note that GC data was typically obtained after 10 min of steady-state current. b: Impact of applied bias on CH_4 conversion and C2 selectivity at 750°C. c: GC data at various operating temperatures. d: Impact of operating temperature on CH_4 conversion and C2 selectivity, at cell voltage of -0.93 V.

The impact of methane flow rate was determined at 750°C and cell voltage of -0.93 V, Fig. S4. With lower flow rate (longer residence time), the concentration of ethane and ethylene increased and higher hydrocarbons can be produced. Propylene (C_3H_6) was also produced at a low CH_4 flow

rate of 40 cm^2 min^{-1}. In a separate cell with CH_4 flow rate of 30 cm^3 min^{-1} at 750°C and cell voltage of -0.93V, several light olefins (6% C_2H_4, 1.5% C_3H_6, and 0.2% C_4H_8) and paraffins (3.8% C_2H_6) were produced (Fig. 5b). Faradaic efficiency for C_2H_4, C_2H_6, C_3H_6, and C_4H_8 were 42.8%, 27.2%, 16.1%, and 3.3% respectively. The total Faradaic efficiency for ≥C2 reached 89.4±4.5% (Table S1), which is close to the 92% reported by Zhu et al [9] and higher than a recently reported value (~ 70%) by Ramaiyan et al [43]. Higher hydrocarbon (C5+) were not observed by GC. Hydrogen was also produced as the by-product of OCM (Eq. 4), and 42% H_2 was detected in the exhaust gas; this hydrogen was not consumed due to low HOR (Eq. 1) activity of SFM. As a side note, an increased amount of propene was produced when pure oxygen (instead of air) was flowing at the oxygen electrode (Fig. S5). The highest ethylene selectivity (35.5%) was observed for a similar cell at 800°C (Fig 5a). The C_2H_4 and C_2H_6 concentration reached 10.5% and 12.3%, respectively, with CH_4 conversion of 85.8% and ≥C2 selectivity of 71.6% (Table S2), which are higher than typical OCM reaction (CH_4 conversion of 1-12.4%, and C2 selectivity of 23-58%)[44]. The C_2H_4/C_2H_6 ratio (1:1.2) is significantly improved compared to the other results discussed above at 750°C. It is encouraging that these MS-SOC results are comparable to previous work with conventional E-OCM cell designs. Our total C_2H_4 and C_2H_6 products at 800°C (22.8%) are slightly higher than reported C2 concentration of 16.7% (12.1% of ethylene and 4.6% ethane) at a higher operating temperature of 850°C [9]. Our ethylene selectivity (35.5%) at 800°C is lower than those of Zhu et al[9] (81.2%) and Ramaiyan, et al. [39] (82.2%) (both proceeded at 850°C) due to a lower temperature in the E-OCM reaction. A higher operating temperature promotes ethane dehydrogenation on iron/SFM catalyst to form ethylene and thus increases the selectivity to ethylene. Higher operating temperature is, however, not compatible with long-term oxidation of the metal support used here.

The post-test adsorbed species on the SFM electrode of the cell shown in Fig. 5b was analyzed by Raman spectroscopy. Multiple points on the sample were analyzed with 2 lasers: 488 nm to observe carbon species and 633 nm to observe SFM phases. Spectra collected with 633 nm contain three peaks around 794, 842, 884 cm^{-1}, which were assigned to $SrMoO_4$ phase (PDF-085-0586) [45] (Fig. 5c). Two peaks around 320 and 620 cm^{-1} were assigned to perovskite $Sr_2FeMoO_{6-\delta}$ (PDF: 060-0459) [46]. Above approximately 1300 cm^{-1}, photoluminescent background was present and therefore carbon and hydrocarbon species were analyzed using the 488 nm laser. The laser has significantly lower penetration depth compared to 633 nm, therefore peaks of $SrMoO_4$ and $Sr_2FeMoO_{6-\delta}$ were diminished. On the other hand, surface hydrocarbon species have strong features. A peak around 1660 cm^{-1} is assigned to C=C bond, a peak at 2202 cm^{-1} is assigned to adsorbed C4 species, and a peak at 2493 cm^{-1} is assigned to aromatic-CH_3 [47]. Minimal surface carbon is also detected. A shoulder at ~1550 cm^{-1} corresponds to G peak from graphitic carbon excited at 488 nm [48]. No peak from amorphous carbon was observed (1350 cm^{-1}). Different ratios of hydrocarbon vs $SrMoO_4$ and $Sr_2FeMoO_{6-\delta}$ were observed across the sample, which is an indication of various adsorbed intermediate hydrocarbon species (Figs. 5c, S6). Featureless spectra are also possible, and arise from the ScSZ support area due to beam shift away from the SFM area (Fig S6b).

.

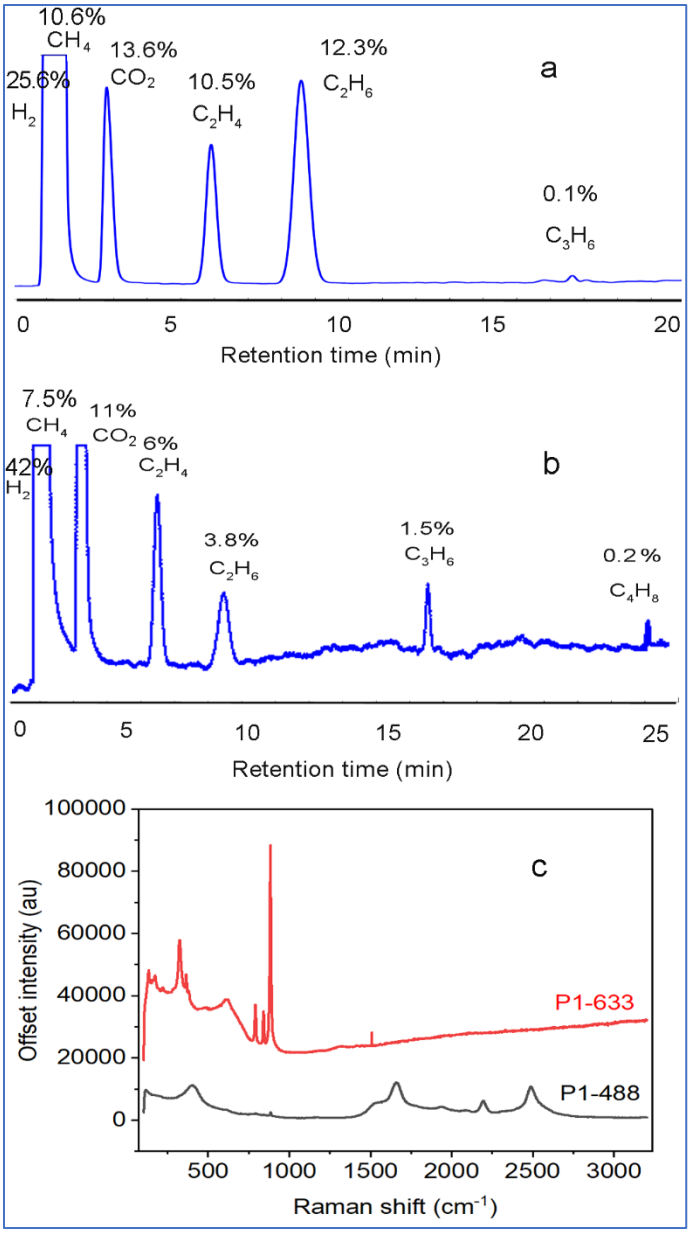

Fig. 5. Exemplary E-OCM product synthesis and Raman spectra of post-test SFM electrode. Inlet methane fuel compositions: 80% CH_4/10%/Ar/10% H_2O. GC spectra of E-OCM reaction products with a: CH_4 flow rate of 120 cm^3 min^{-1}, 800°C, -0.93 V cell voltage, oxygen flowrate of 1200 cm^3 min^{-1}, b: CH_4 flow rate of 30 cm^3 min^{-1}, 750°C, -0.93 V cell voltage; and c: Raman spectra of post-test cell (three points in the middle of the sample) shown in b.

3.4 Cell stability and post-operation characterization

An MS-SOC with SFM anode maintained good stability during 200 h E-OCM operation at an intermediate temperature of 750°C (Fig. 6). The cell showed relatively stable performance with a moderate initial current density around 600 mA cm^{-2}, and an average degradation rate of 4.3% per 100 h. Methane conversion around 50% was maintained throughout the testing period. This stability is similar to that reported by Zhu, et al. [9]. The degradation here is slower than for MS-SOFCs with Ni-ceria infiltrated anode operating with hydrocarbon fuel, where the initial degradation rate is 10 to 15%/100 h[37].

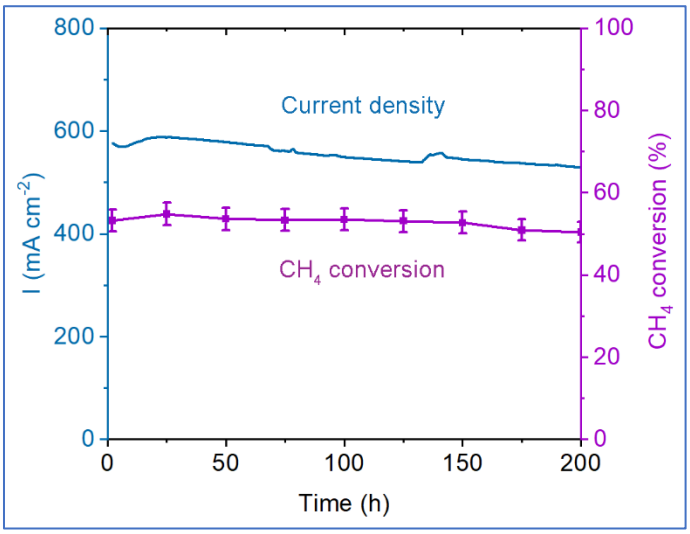

Fig. 6. Cell stability. Potentiostatic operation of an MS-SOC with SFM anode at 750°C and cell voltage of -0.93 V with methane fuel and air. Inlet methane fuel compositions: 80% CH_4/10%/Ar/10% H_2O.

The full cell structure (sintered, without catalysts), and the electrochemically active layers (with catalysts) after operation are shown in Fig 7. After 200 h operation, no carbon deposition was observed in the pores of the SFM anode (Fig. 7c), or on the metal support. The Pr_6O_{11} cathode catalyst remained porous and well-connected (Fig. 7d). Both catalysts remained sub-micron with

minimal coarsening. This is in contrast to previous results for infiltrated Ni-ceria anode, where extensive coarsening of the Ni was observed [37]. In addition to catalyst coarsening, Cr deposition at the cathode contributes to degradation (Fig. S7). To further improve the cell stability, a Cr-blocking coating can be applied to the metal support at the cathode [49]. It was previously noticed that a secondary phase ($SrZrO_3$) forms in the mixture of SFM and YSZ after firing at 1000 °C for 24 h in air [35]. Our SFM infiltration and firing temperature were processed at a low temperature at a short time (850°C, 0.5 h per cycle). No XRD peaks of $SrZrO_3$ were observed for a posttest SFM-ScSZ anode (Figs. 7e). Further experiments confirmed that no obvious secondary phase of $SrZrO_3$ was observed after 100-hour reduction at 850°C in mixture of 50 :50 wt% SFM and ScSZ (Fig. S8). The posttest SFM-ScSZ XRD pattern is similar to those of ex-situ SFM powders (Fig. 2b). Three phases (Fe_3O_4, $SrMoO_4$, and $Sr_2FeMoO_{6-\delta}$) are shown. Small peaks of $SrCO_3$ were shown in the posttest SFM electrode but the intensity of these peaks is much lower than reported results in Ramaiyan et al [50], indicating less SrCO3 formation. Overall, Raman spectra, SEM images, and XRD data demonstrated carbon resistive SFM electrode, phase stability, and mitigation of SrCO3 formation, which support the good cell stability.

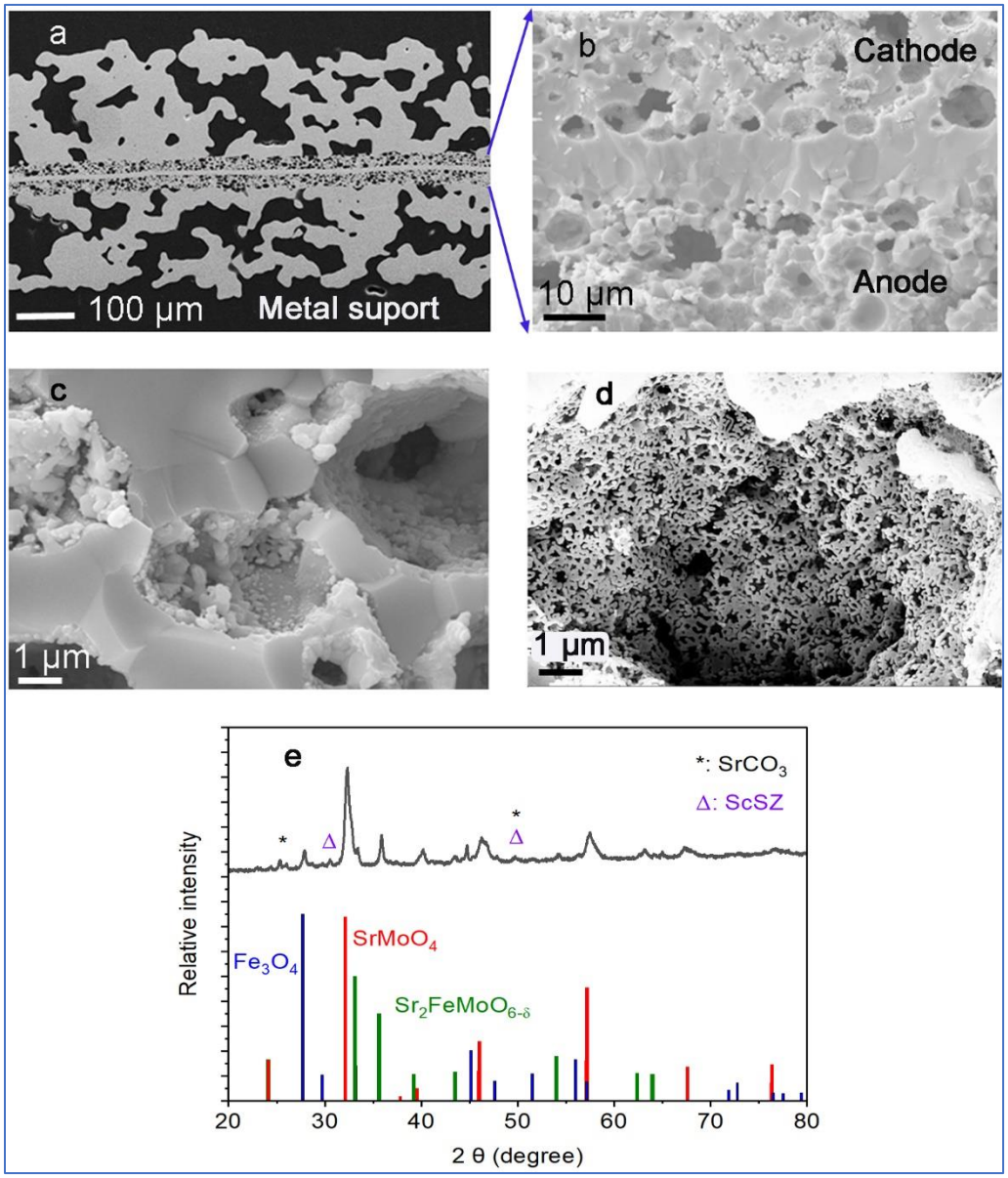

Fig. 7 Cell and catalyst structure. a: Sintered MS-SOCs without catalysts. b: posttest Pr_6O_{11}-ScSZ‖ScSZ‖ScSZ-SFM, c: post-test SFM in porous ScSZ, d: Posttest Pr_6O_{11} in porous ScSZ. e: XRD pattern of a E-OCM posttest (200 h test in methane fuel) SFM electrode after metal support was removed.

4. Conclusions

The MS-SOC with infiltrated SFM anode catalyst has been developed by optimizing the selection of chelating agents, firing/reducing temperature, and metal support structure. Citric acid/EG was selected as the best chelating agent for dissolution and stability of the SFM infiltration precursor solution. Perovskite SFM was obtained upon firing at 900°C in 3% H_2/Ar for 10 h. The firing temperature for full cells was limited to 800°C to avoid over-oxidation of the metal supports. In this case, pure perovskite SFM phase was not achieved, but the catalyst was nevertheless effective for the E-OCM reaction. The effects of process parameters including cell voltage, operating temperature, and CH_4 flow rate were investigated at 650 to 800°C. Methane conversion up to 85.8±4.3% and a C2 selectivity up to 71.6±3.6% were achieved at 800°C. E-OCM is the favored reaction and the selectivity to C2+ reached 75.5±3.8% at a cell voltage of -0.33 V. The highest ethylene content observed in the exhaust gas was 10.5% at 800°C with a cell voltage of -0.93 V, and ethylene selectivity of 35.5%. Hydrogen (42%) was produced as by-product. Higher olefins (C3+) were produced at low methane flow rate and high current density (with O_2 flowing at the cathode). Good stability of the current density and methane conversion was observed during 200 h operation. Post-test characterization shows stable porous electrodes and some Cr deposition at the cathode. It is anticipated that the large overpotentials used here and in previous E-OCM studies present a challenge for economical production of ethylene. A detailed techno-economic analysis to address this issue and provide targets for the electrochemical performance will be presented in a separate study.

Acknowledgements

This work was funded primarily Lawrence Berkeley National Laboratory, via the LDRD program. This work was funded in part by the U.S. Department of Energy under contract no. DE-

AC02-05CH11231. This work was funded in part by the U.S. Department of Energy, Office of Energy Efficiency and Renewable Energy, Advanced Manufacturing and Materials Technologies Office (AMMTO), U.S. Department of Energy under contract number DE-AC02-05CH11231. Work at the Molecular Foundry was supported by the Office of Science, Office of Basic Energy Sciences, of the U.S. Department of Energy under Contract No. DE-AC02-05CH11231. The views and opinions of the authors expressed herein do not necessarily state or reflect those of the United States Government or any agency thereof. Neither the United States Government nor any agency thereof, nor any of their employees, makes any warranty, expressed or implied, or assumes any legal liability or responsibility for the accuracy, completeness, or usefulness of any information, apparatus, product, or process disclosed, or represents that its use would not infringe privately owned rights.

References

[1] Schwach P, Pan X, Bao X. Direct conversion of methane to value-added chemicals over heterogeneous catalysts: challenges and prospects. Chem Rev. 2017;117:8497-520.

[2] Fernández L. Global production capacity of ethylene 2018-2021. https://www.statista.com/statistics/1067372/global-ethylene-production-capacity/2022.

[3] Zhu G, Xie C, Li Z, Wang X. Catalytic process for light olefin production. In: Hsu CS, Robinson PR, editors. Springer handbook of petroleum techology: Springer Cham; 2017. p. 1064-78.

[4] Hu B, Frueh S, Garces HF, Zhang L, Aindow M, Brooks C, et al. Selective hydrogenation of CO_2 and CO to useful light olefins over octahedral molecular sieve manganese oxide supported iron catalysts. Appl Catal B: Environ. 2013;132-133:54-61.

[5] Amghizar I, Vandewalle LA, Van Geem KM, Marin GB. New trends in olefin production. Engineering -Longdon. 2017;3:171-8.

[6] Farrell BL, Igenegbai VO, Linic S. A viewpoint on direct methane conversion to ethane and ethylene using oxidative coupling on solid catalysts. ACS Catal. 2016;6:4340-6.

[7] Luna PD, Haha C, Higgins D, Jaffer SA, Jarmillo TF, Sargent EH. What would it take for renewably powered electrosynthesis to displace petrochemical processes? Science. 2019;364:350.

[8] Kyun Kim S, Kwon Y-i, Beom Kim Y, Jung J, Kang S, Hoon Joo J. Novel approach to integrate CO_2 utilization coupled with direct methane conversion to C2 products using solid oxide electrolysis cell. Chem Eng J. 2022;444.

[9] Zhu C, Hou S, Hu X, Lu J, Chen F, Xie K. Electrochemical conversion of methane to ethylene in a solid oxide electrolyzer. Nat Commun. 2019;10:1173.

[10] Liu K, Zhao J, Zhu D, Meng F, Kong F, Tang Y. Oxidative coupling of methane in solid oxide fuel cell tubular membrane reactor with high ethylene yield. Catal Commun. 2017;96:23-7.

[11] Thyssen VV, Vilela VB, de Florio DZ, Ferlauto AS, Fonseca FC. Direct conversion of methane to C2 hydrocarbons in solid-state membrane reactors at high temperatures. Chem Rev. 2022;122:3966-95.

[12] Morejudo SH, Zanón R, Escolástico S, Yuste-Tirados I, Malerød-Fjeld H, Vestre PK, et al. Direct conversion of methane to aromatics in a catalytic co-ionic membrane reactor. Science. 2016;353:563.

[13] Ding D, Zhang Y, Wu W, Chen D, Liu M, He T. A novel low-thermal-budget approach for the co-production of ethylene and hydrogen via the electrochemical non-oxidative deprotonation of ethane. Energ Environm Sci. 2018;11:1710-6.

[14] Fu XZ, Luo JL, Sanger AR, Danilovic N, Chuang KT. An integral proton conducting SOFC for simultaneous production of ethylene and power from ethane. Chem Commun (Camb). 2010;46:2052-4.

[15] Feng Y, Luo J, Chuang KT. Conversion of propane to propylene in a proton-conducting solid oxide fuel cell. Fuel. 2007;86:123-8.

[16] Zhou M, Liu Z, Yan X, Tan K, Tian F, Liu J. Simultaneous electrochemical reduction of carbon dioxide and partial oxidation of methane in a solid oxide cell with silver-based cathode and nickel-based anode. J Electrochem Soc. 2022;169.

[17] Shi N, Xue S, Xie Y, Yang Y, Huan D, Pan Y, et al. Co-generation of electricity and olefin via proton conducting fuel cells using $(Pr_{0.3}Sr_{0.7})_{0.9}Ni_{0.1}Ti_{0.9}O_3$ catalyst layers. Appl Catal B: Environ. 2020;272.

[18] Li Y, Chen X, Yang Y, Jiang Y, Xia C. Mixed-Conductor $Sr_2Fe_{1.5}Mo_{0.5}O_{6-\delta}$ as Robust fuel electrode for pure CO_2 reduction in solid oxide electrolysis cell. ACS Sustain Chem Eng. 2017;5:11403-12.

[19] Wang L, Fan Y, Li J, Shao L, Xi X, Fu X-Z, et al. $La_{0.5}Sr_{0.5}Fe_{0.9}Mo_{0.1}O_{3-\delta}$-$CeO_2$ anode catalyst for co-producing electricity and ethylene from ethane in proton-conducting solid oxide fuel cells. Ceram Int. 2021;47:24106-14.

[20] Munoz-Garcia AB, Bugaris DE, Pavone M, Hodges JP, Huq A, Chen F, et al. Unveiling structure-property relationships in $Sr_2Fe_{1.5}Mo_{0.5}O_{6-\delta}$, an electrode material for symmetric solid oxide fuel cells. J Am Chem Soc. 2012;134:6826-33.

[21] Sun N, Jin F, Liu X, Liu X, Li J, Shen Y, et al. In situ coexsolution of metal nanoparticle-decorated double perovskites as anode materials for solid oxide fuel cells. ACS Appl Energ Mater. 2021;4:7992-8002.

[22] Tucker MC, Ying AS. Metal-supported solid oxide fuel cells operated in direct-flame configuration. Int J Hydrogen Energy. 2017;42:24426-34.

[23] Tucker MC. Durability of symmetric-structured metal-supported solid oxide fuel cells. J Power Sources. 2017;369:6-12.

[24] Hamedi M, Omidkhah M, Sadrameli SM, Khoshgoftar Manesh MH. Exergetic, exergoeconomic, and exergoenvironmental analyses of an existing industrial olefin plant. Sustain Energy Technol Assess. 2022;52.

[25] Karimzadeh R, Godini HR, Ghashghaee M. Flowsheeting of steam cracking furnaces. Chem Eng Res Des. 2009;87:36-46.

[26] Lau GY, Tucker MC. Development of metal-supported proton-conducting solid oxide cells via co-sintering. ECS Trans. 2021;103:685-92.

[27] Tucker MC, Lau GY, Jacobson CP, DeJonghe LC, Visco SJ. Performance of metal-supported SOFCs with infiltrated electrodes. J Power Sources. 2007;171:477-82.

[28] Hu B, Lau G, Song D, Fukuyama Y, Tucker MC. Optimization of metal-supported solid oxide fuel cells with a focus on mass transport. J Power Sources. 2023;555.

[29] Osinkin DA, Beresnev SM, Bogdanovich NM. Influence of Pr_6O_{11} on oxygen electroreduction kinetics and electrochemical performance of $Sr_2Fe_{1.5}Mo_{0.5}O_{6-\delta}$ based cathode. J Power Sources. 2018;392:41-7.

[30] Li J, Zhao X, Min H, Lu Y, Li M, Ding X. Enhancing oxygen reduction activity and CO_2-tolerance of A-site-deficient $BaCo_{0.7}Fe_{0.3}O_{3-\delta}$ cathode by surface-decoration with Pr_6O_{11} particles. Int J Hydrogen Energy. 2020;45:31070-9.

[31] Dogdibegovic E, Wang R, Lau GY, Tucker MC. High performance metal-supported solid oxide fuel cells with infiltrated electrodes. J Power Sources. 2019;410-411:91-8.

[32] Dogdibegovic E, Cheng Y, Shen F, Wang R, Hu B, Tucker MC. Scaleup and manufacturability of symmetric-structured metal-supported solid oxide fuel cells. J Power Sources. 2021;489.

[33] Shen F, Welander MM, Tucker MC. Metal-supported solid oxide electrolysis cell test standard operating procedure. Front Energ Res. 2022;10.

[34] Wang R, Dogdibegovic E, Lau GY, Tucker MC. Metal-supported solid oxide electrolysis cell with significantly enhanced catalysis. Energy Technol. 2019;7.

[35] Liu Q, Dong X, Xiao G, Zhao F, Chen F. A novel electrode material for symmetrical SOFCs. Adv Mater. 2010;22:5478-82.

[36] Yang Y, Yang Z, Chen Y, Chen F, Peng S. A promising composite anode for solid oxide fuel cells: $Sr_2FeMo_{0.65}Ni_{0.35}O_{6-\delta}$-$Gd_{0.1}Ce_{0.9}O_{2-\delta}$. J Electrochem Soc. 2019;166:F109-F13.

[37] Welander MM, Hu B, Tucker MC. Metal-supported solid oxide fuel cells operating with reformed natural gas and sulfur. Inter J Hydrogen Energy. 2022;47:11261-9.

[38] Welander MM, Hu B, Belko S, Lee KX, Dubey PK, Robinson I, et al. Direct utilization of gaseous fuels in metal supported solid oxide fuel cells. Inter J Hydrogen Energy. 2023;48:1533-9.

[39] Ramaiyan KP, Denoyer LH, Benavidez A, Garzon FH. Selective electrochemical oxidative coupling of methane mediated by Sr2Fe1.5Mo0.5O6-δ and its chemical stability. Commun Chem. 2021;4.

[40] Ciucci F, Chen C. Analysis of electrochemical impedance spectroscopy data using the distribution of relaxation times: a Bayesian and hierarchical Bayesian approach. Electrochim Acta. 2015;167:439-54.

[41] Xu Z, Hu X, Wan Y, Xue S, Zhang S, Zhang L, et al. Electrochemical performance and anode reaction process for Ca doped $Sr_2Fe_{1\cdot5}Mo_{0\cdot5}O_{6-\delta}$ as electrodes for symmetrical solid oxide fuel cells. Electrochim Acta. 2020;341.

[42] Song Y, Lin L, Feng W, Zhang X, Dong Q, Li X, et al. Interfacial enhancement by gamma-Al_2O_3 of electrochemical oxidative dehydrogenation of ethane to ethylene in solid oxide electrolysis cells. Angew Chem Int Ed Engl. 2019;58:16043-6.

[43] Ramaiyan KP, Denoyer LH, Benavidez A, Garzon FH. Electrochemical oxidative coupling of methane to produce higher hydrocarbons using $Sr_2Fe_{1.5}Mo_{0.5}O_{6-\delta}$ electrocatalysts. 2021.

[44] Alexiadis VI, Chaar M, van Veen A, Muhler M, Thybaut JW, Marin GB. Quantitative screening of an extended oxidative coupling of methane catalyst library. Appl Catal B: Environ. 2016;199:252-9.

[45] Muralidharan M, Anbarasu V, Elaya Perumal A, Sivakumar K. Enhanced ferromagnetism in Cr doped SrMoO4 scheelite structured compounds. J Mater Sci Mater Electron. 2015;27:2545-56.

[46] Xu ZF, Zhang Q, Yuan SJ. Detection of phase purity of Sr_2FeMoO_6 by Raman spectroscopy. Adv Mater Res. 2014;989-994:130-3.

[47] Lucotti A, Tommasini M, Fazzi D, Zoppo MD, Chalifoux WA, Ferguson MJ, et al. Evidence for solution-state nonlinearity of sp-sarbon chains based on IR and Raman spectroscopy: violation of mutual exclusion. J Am Chem Soc. 2009;131:4239-44.

[48] Ferrari AC, Robertson J. Resonant Raman spectroscopy of disordered, amorphous, and diamondlike carbon. Phys Rev B. 2001;64.

[49] Shen F, Reisert M, Wang R, Singh P, Tucker MC. Assessment of protective coatings for metal-supported solid oxide electrolysis cells. ACS Appl Energ Mater. 2022;5:9383-91.

[50] Ramaiyan KP, Denoyer LH, Benavidez A, Garzon FH. Selective electrochemical oxidative coupling of methane mediated by $Sr_2Fe_{1.5}Mo_{0.5}O_{6-\delta}$ and its chemical stability. Commun Chem. 2021;4.